CHEMISTRY OF MATERIALS

Article

pubs.acs.org/cm

Synthesis of Si_xGe_{1-x} Nanocrystals Using Hydrogen Silsesquioxane and Soluble Germanium Diiodide Complexes

Stephen D. Barry, Zhenyu Yang, Joel A. Kelly, Eric J. Henderson,[†] and Jonathan G. C. Veinot*

Department of Chemistry, University of Alberta, Edmonton, Alberta, Canada T6G 2G2

Supporting Information

ABSTRACT: We report an investigation into the formation of Si_xGe_{1-x} alloy nanocrystals ($64 < x < 100$) synthesized from mixing GeI_2:PR_3 adducts with hydrogen silsesquioxane (HSQ). The use of trialkylphosphine adducts allows GeI_2 and HSQ to be homogeneously coprecipitated, improving control over the size and composition of the resulting Si_xGe_{1-x} nanocrystals. This approach yields oxide-embedded and freestanding materials with near-infrared photoluminescence (PL) comparable in quantum efficiency to similarly prepared Si nanocrystals. The formation of bimodal populations of Si-rich and Ge-rich nanocrystals was observed, with homogeneous distribution of Ge within each population. Through changes to precursor stoichiometry and annealing temperature and time, control over particle size and composition was demonstrated. The impact of these factors on the near-IR PL was evaluated. We propose a multistep formation mechanism to account for the formation of separate Si-rich and Ge-rich populations and present indirect evidence for the participation of Ge in the emission process. Materials were analyzed using Fourier transform infrared spectroscopy, Raman spectroscopy, powder X-ray diffraction, PL spectroscopy, high-resolution transmission electron microscopy and spatially resolved energy-dispersive X-ray spectroscopy.

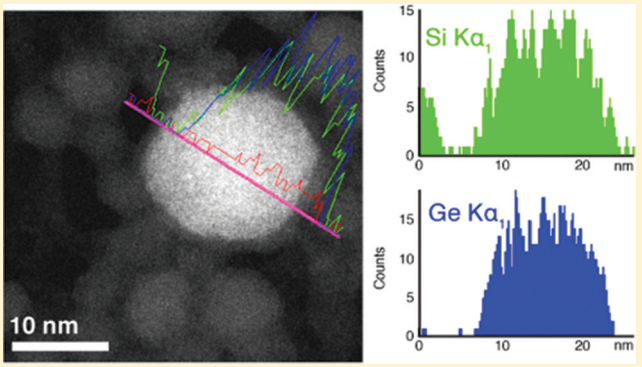

KEYWORDS: *Si_xGe_{1-x}, nanoparticle, quantum confinement, photoluminescence, bandgap engineering*

INTRODUCTION

Achieving control over the bandgap of semiconductor nanocrystals (NCs) is an important goal for numerous emerging technologies utilizing these materials, including near-infrared (IR) biological tags[1] and nonvolatile memory devices.[2,3] Tailoring particle size can afford control over NC bandgaps by exploiting quantum size effects and is well-established.[4,5] Compositional modifications have also drawn substantial interest for tailoring optoelectronic properties through the incorporation of isovalent elements (e.g., $Cd_xZn_{1-x}Se$,[6] CdS_xSe_{1-x},[7,8] $HgSe_xS_{1-x}$,[9] CdS_xTe_{1-x}[10]). These ternary compound semiconductors exhibit electronic properties intermediate to the parent binary semiconductors. The additional degree of freedom provided by NC compositional tailoring is particularly appealing because it allows for bandgap modification without some of the challenges associated with changing particle size. For example, CdSe NCs emitting in the blue spectral region often exhibit increased reactivity and limited stability due to their small size (i.e., $d < 2$ nm), Larger $Zn_xCd_{1-x}Se$-NCs (i.e., $d \approx 7.5$ nm) exhibit highly stable blue emission.[11,12] Tailoring NC composition may also yield unique optoelectronic properties that arise from compositionally induced structural changes (e.g., homogeneously alloyed, core−shell, or gradient compositions). For example, graded core−shell alloy $Zn_xCd_{1-x}Se/ZnSe$-NCs are immune to photoluminescence "blinking" where NC emission is intermittently quenched by the presence of charged excited states.[13−15]

For Group 14 materials, solid solutions of Si and Ge have received attention for tuning the material bandgaps in thin films and bulk morphologies.[16−18] Si and Ge form a disordered solid solution and are 100% miscible in the solid state (i.e., Si_xGe_{1-x}, $0 \le x \le 1$). Photoluminescence (PL) from Si_xGe_{1-x}-NCs has also drawn substantial interest; it has been proposed the random distribution of Si and Ge within the alloy may break the translational symmetry that gives rise to the indirect bandgaps in pure Si and Ge.[19,20] This could increase the extinction coefficient, radiative recombination rate, and photoluminescent quantum yield of Si_xGe_{1-x}-NC. Theoretical studies on Si_xGe_{1-x} clusters have also suggested the distribution of Si and Ge atoms within these NCs (i.e., core−shell particles or other morphologies) could significantly impact their optoelectronic properties.[21−23]

Nanostructured Si_xGe_{1-x} has been prepared using several methods, including ion implantation, physical and chemical vapor deposition,[16] molecular beam epitaxy,[24,25] radio frequency cosputtering,[20,26] nonthermal plasma pyrolysis,[27] and thermal suboxide disproportionation.[28] Each of these

Received: September 15, 2011
Revised: October 7, 2011
Published: October 20, 2011

Table 1. Synthesis Conditions and Percent Ge Composition of Si_xGe_{1-x} Solid Solution Nanoparticles

sample code	binding ligand	temp. (°C)	time (h)	HSQ:GeI_2 ratio[a]	Ge-rich size (nm)[b]	Si-rich size (Si, nm)[b]	Ge-rich composition (% Ge)[c]
A	TOP	1100	5	4.73	17	14	69 ± 1
B	TOP	1050	5	4.73	15	8	66 ± 1
C	TOP	1000	5	4.73	14	7	70 ± 1
D	TOP	900	5	4.73	12	9	81 ± 1
E	TOP	800	5	4.73	9	8	75 ± 1
F	TBP	1100	5	4.73	12	5	68 ± 1
G	TBP	1050	5	4.73	14	4	74 ± 4
H	TBP	1000	5	4.73	22	4	78 ± 1
I	TBP	1100	1	4.73	13	3	71 ± 2
J	TBP	1100	3	4.73	17	4	75 ± 1
F	TBP	1100	5	4.73	12	5	68 ± 1
K	TBP	1100	7	4.73	12	4	74 ± 1
L	TBP	1100	9	4.73	13	5	74 ± 2
M	TBP	1100	5	1.35	16	5	76 ± 1
N	TBP	1100	5	2.70	20	6	86 ± 1
F	TBP	1100	5	4.73	12	5	68 ± 1
O	TBP	1100	5	6.75	14	4	64 ± 1

[a]Calculated by weight. [b]Particle size estimated using Scherrer analysis. [c]Composition estimated using a modified version of Vegard's law using XRD lattice constants.

techniques has associated benefits and challenges. Factors that must be considered for a specific application include process scalability, product yield, energy input, crystallinity, polydispersity, and surface chemistry. Our group has explored the simultaneous thermal disproportionation of GeI_2 with hydrogen silsesquioxane (HSQ) to form Si_xGe_{1-x}-NCs.[28] HSQ offers several advantages as a precursor for oxide-embedded and freestanding Si-NCs, yielding well-defined NCs whose PL can be controlled throughout the visible and near-IR spectral regions.[29] The challenges associated with its use as a Si precursor with GeI_2 for Si_xGe_{1-x} NCs included the formation of bulk Ge as a byproduct, low yields, and a lack of compositional and size control. No PL was observed, likely a result of the relatively large size of NCs produced. The majority of these concerns result from macroscopically inhomogeneous distribution of precursors due to the solid-state grinding approach taken, which requires large excesses of GeI_2 to form the desired alloy.

Here we present a strategy to overcome the issue of inhomogeneous mixing by rendering "GeI_2" soluble in HSQ compatible solvents via the formation of trialkylphosphine adducts (i.e., R_3P:GeI_2). This approach allows straightforward coprecipitation of HSQ and GeI_2 from solution to form a homogeneous precursor of varied Si:Ge ratios. Following annealing, the resulting oxide composites contain Si-rich and Ge-rich NCs rather than excess bulk Ge, and exhibit bright near-IR PL. The impact of processing temperature, processing time, processing atmosphere, trialkylphosphine chain length, and GeI_2:HSQ stoichiometry on the size and composition of the resulting materials has been explored. These studies provide detailed insight into the formation mechanisms from these hybrid precursors. As well, the oxide matrix could be removed using hydrofluoric acid (HF) etching and the resulting freestanding hydride-terminated particles functionalized through thermal hydrosilylation/hydrogermylation. Characterization by high-resolution electron microscopy, high-angle angular dark-field imaging and energy-dispersive X-ray spectroscopy linescaning confirmed the presence of homogeneously alloyed Si_xGe_{1-x}-NCs. The near-IR PL and quantum yield was evaluated in the context of the presence of both Si-rich and Ge-rich NCs.

EXPERIMENTAL METHODS

Reagents and Materials. Tri-n-octylphosphine (TOP, 97%, Sigma-Aldrich), tri-n-butylphosphine (TBP, 97% Sigma-Aldrich), HSQ (trade name FOx-16, Dow Corning) in methylisobutylketone (MIBK), and hydrofluoric acid (HF, 49%, electronics grade, J.T. Baker), were used as received. Germanium diiodide (GeI_2, 99.9%, Strem Chemicals, Inc.) was purified upon mixing with benzene and filtering off any halogen or germanium tetraiodide impurities under Ar. 1-Dodecene was purified by passing over neutral alumina to remove peroxide impurities.[30]

Preparation of Si−Ge/SiO_2 Composite. GeI_2 (ca. 1.2 mmol) was added to 10 mL of TOP or TBP, forming a bright yellow saturated solution. A portion of this solution was mixed with FOx-16 in MIBK to a balance of 10 mL and stirred for 1 h, turning a deep red. The solvent was removed under vacuum overnight yielding a red solid that was transferred to a quartz boat, placed in a flowing gas tube furnace (Lindberg/Blue TF55035A), and heated at 18 °C/min to the desired processing temperature for 1−9 h. Following cooling to room temperature, the glassy brown composite powder was ground using an agate mortar and pestle into a fine powder. Processing conditions and sample codes are listed in Table 1.

Liberation of Freestanding Nanocrystals. Composites were HF etched to liberate freestanding nanocrystals. Briefly, 0.3 g of the ground composite was added to 7 mL of a 49% HF solution and stirred for 5 min. Three milliliters of anhydrous ethanol was added to aid surface wetting of the hydrophobic materials, and the mixture stirred for a further 2 min, forming hydrophobic, hydride-terminated NCs. The freestanding particles were extracted into two 15 mL aliquots of toluene as a cloudy, brown dispersion.

Surface Functionalization of SiGe Nanocrystals. The organic extracts were combined into glass test tubes and centrifuged at 3000 rpm to precipitate the NCs. The toluene was decanted and the precipitate resuspended in ca. 10 mL of 1-dodecene and transferred to a Schlenk flask and repeatedly degassed by evacuating and refilling under an Ar atmosphere. Hydrosilylation/hydrogermylation was carried out at 190 °C for 15 h by heating in a silicone oil bath. The reaction mixture changed from turbid brown to clear orange/red within the first 3 h of heating.

The reaction mixture was cooled to room temperature and centrifuged at 3000 rpm. The supernatant was filtered through a 250 nm PTFE filter to remove agglomerated material. The filtered

dx.doi.org/10.1021/cm202761k|Chem. Mater. 2011, 23, 5096−5103

supernatant containing functionalized NCs was purified via three precipitation/resuspension cycles using hexanes (solvent) and 1:3 methanol:anhydrous ethanol (antisolvent), centrifugation (20 min at 25 900 G), and resuspension. Purified particles were dispersed in hexanes and stored under ambient conditions until further use.

Material Characterization. X-ray powder diffraction (XRD) was performed using an INEL XRG 3000 X-ray diffractometer equipped with a Cu K_α radiation source (λ = 1.54 Å). Composite crystallinity was evaluated on finely ground samples mounted on a polycarbonate sample holder. The lattice constants were determined by fitting the obtained diffraction peaks with the theoretical peaks of a diamond crystal structure.

Raman spectroscopy was performed on powder samples using a Renishaw inVia Raman microscope with a 785 nm diode laser and a power of 7.94 mW on the sample. The composite samples were not visibly affected by the incident radiation. Fourier transform IR spectra were collected using a Nicolet Magna 750 IR spectrometer on drop-cast films.

Photoluminescence spectra were collected at room temperature using the 457 nm line of an ArKr ion laser operated with a continuous-wave power of 30 mW. Emission was detected using fiber-optic coupled Ocean Optics USB2000 charge coupled device spectrometer whose spectral response was normalized using a standard blackbody radiator. Samples were prepared by drop casting onto silicon wafers (composites were first finely ground and suspended in ethanol).

Absolute PL quantum yields (Φ_{PL}) of functionalized samples were measured in a LabSphere integrating sphere, with 600 nm excitation from a Xenon lamp passed through a monochromator (PTI). The emission and excitation spectra were collected with a Si charge-coupled device (CCD) detector. Full experimental details have been reported elsewhere.[31] Φ_{PL} of freshly prepared samples in hexane (diluted to an approximate optical transmittance of 95%) were determined by integrating four spectral scans of the sample and of the reference cuvette containing solely hexane through the relation

$$\Phi_{PL} = \frac{\int I_{sample}(\lambda)d\lambda}{\int E_{ref}(\lambda) - E_{sample}(\lambda)d\lambda} \quad (1)$$

where E_{ref} is the transmitted intensity of the 600 nm light measured for the reference cuvette, E_{sample} is the transmitted intensity of the 600 nm light of the sample, and I_{sample} is the integrated PL intensity. This approach yields reasonable values for reference dyes commonly used for relative quantum yield determination.[31] For the TBP-prepared sample that exhibited near-IR PL extending beyond the Si CCD detector limit, the obtained Φ_{PL} is considered a lower limit.

High resolution transmission electron microscopy (HRTEM) was performed at the Brockhouse Institute for Materials Research (BIMR) at McMaster University using a Titan^3 G2 60−300 TEM operating at 300 kV. High-angle annular dark-field (HAADF) images and energy dispersive X-ray spectroscopy (EDS) line scans were acquired with a FEI Titan 80−300 operated at 300 kV and equipped with a spherical aberration corrector on the imaging lens. All the spectral acquisition and data analysis were carried out using the Inca EDXS software provided by Oxford Instruments. Prior to analysis, functionalized samples were purified through two additional solvent/antisolvent cycles and resuspended in chloroform to fully remove any organic species that might have hindered analysis through electron-beam induced decomposition. Samples were drop coated from a dilute chloroform dispersion onto a carbon-coated copper grid (SPI supplies).

RESULTS AND DISCUSSION

Synthesis of alloy NCs using simultaneous decomposition of multiple precursors presents an intriguing challenge because nucleation and growth processes involving both precursors must be controlled/coordinated if the desired alloy particles are to be prepared. For a homogeneous alloy, the decomposition of the Si and Ge precursors must be similar, and the solubility of both precursors must allow for facile mixing to prevent formation of unalloyed NCs. To achieve this type of Ge incorporation into Si-NCs formed from HSQ requires a precursor that decomposes to produce elemental Ge at approximately the same temperature HSQ yields elemental Si (ca. 350 °C),[32] does not produce substantial carbonaceous impurities upon thermal decomposition that could inhibit nanocrystal growth or liberation,[33] and is soluble in methylisobutylketone (MIBK) or toluene to allow homogeneous coprecipitation with HSQ.

GeI_2 satisfies all but one of these criteria. It thermally disproportionates at ∼330 °C to generate $Ge^{(0)}$ and GeI_4 as a volatile byproduct.[34] Unfortunately, GeI_2 is sparingly soluble in MIBK and toluene, limiting homogeneous mixing with HSQ and thus control over NC composition and size. This issue may be addressed by forming GeI_2 adducts with phosphine ligands (e.g., TOP and TBP), first studied by King in 1963.[35] The increased solubility of these species in organic solvents has been studied in the solution-phase syntheses of Ge nanocrystals.[36] It is reasonable that the increased solubility can also facilitate mixing with HSQ to give an intimately mixed precursor. Adding to the appeal of these new Ge precursors, King's initial report noted decomposition proceeded via dissociation of the phosphine ligand, which can be effectively removed via evaporation during present thermal processing.

Raman spectra of all composites reported herein show Ge−Ge, Si−Ge, and Si−Si optical phonons at 288, 389, and 509 cm^{-1} respectively, qualitatively consistent with formation of a Si_xGe_{1-x} solid solution (Figure 1). The relative intensities of

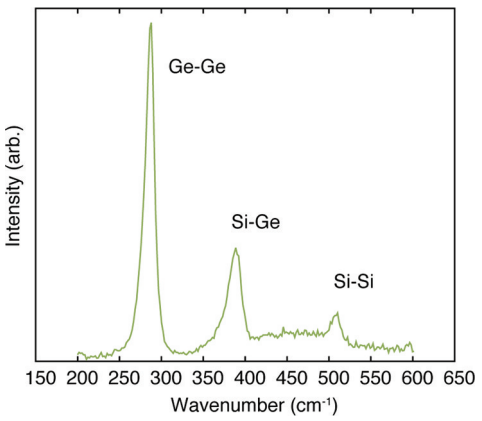

Figure 1. Representative Raman spectra of composite sample M.

these features were not used to estimate particle size or composition due to the heterogeneous nature of the samples (vide infra). XRD patterns show two sets of broad reflections arising from oxide-embedded nanocrystalline domains (Figure 2, for complete XRD patterns of all oxide composites see Figure S1 in the Supporting Information). HSQ processed with TOP:GeI_2 at 1100 °C exhibits reflections at approximately 28.4, 47.3, and 56.1°, resembling Si (111), (220), and (311) reflections, respectively (a_{Si} = 5.4309, ICSD #652265). A second set of reflections at approximately 27.9, 46.3, and 54.9° are arise from a diamond-type structure with lattice constant intermediate to bulk silicon and germanium (a_{Ge} = 5.6569 nm, ICSD #76267) consistent with the formation of nanocrystalline Si_xGe_{1-x} solid solutions. No pure crystalline Ge domains were detected at the sensitivity of the XRD technique.

dx.doi.org/10.1021/cm202761k|Chem. Mater. 2011, 23, 5096−5103

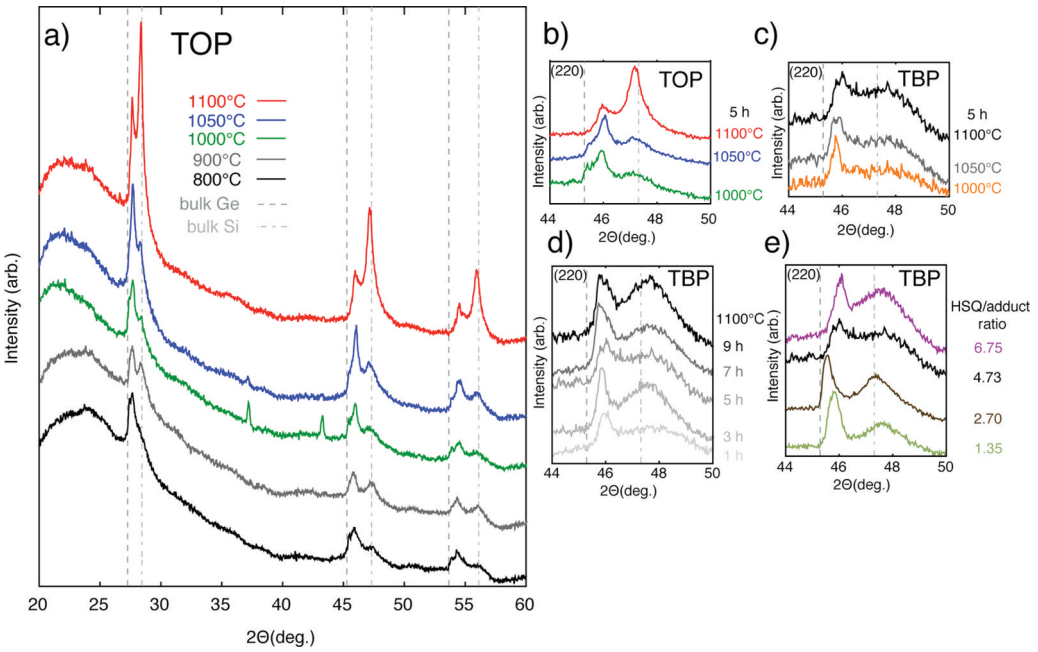

Figure 2. (a) X-ray diffraction patterns of composite samples prepared with TOP between 800 and 1100 °C (A–E). Peaks appearing at 37 and 43° are due to the sample holder. Reflections corresponding to bulk Si and Ge are included to guide the eye. (b) Expanded (220) region for TOP-prepared samples from 1000 to 1100 °C (A–C). (c) Expanded (220) region for TBP-prepared samples from 1000 to 1100 °C (F–H). (d) Expanded (220) region for TBP-prepared samples at 1100 °C for 1–9 h (I–L). (e) Expanded (220) region for TBP-prepared samples at 1100 °C with varying HSQ loading (M–O).

The Ge content of the Si_xGe_{1-x} domains was calculated using an empirically modified version of Vegard's law (equation S1 in the Supporting Information, calculated lattice parameters are listed in Supporting Information, Table S1). Samples prepared using TOP (A-E) and TBP (F–H) decrease in Ge content with increasing temperature. Ge content decreases from 81 to 66% and 78 to 68% for TOP- and TBP-prepared samples, respectively (Table 1). Increasing the loading of TBP:GeI_2 increased the relative intensity of the Si_xGe_{1-x} reflections compared to those of Si and a shift to higher Ge composition (samples M-O, F, Figure 2e). These shifts in composition are consistent with two competing processes: the loss of Ge through evaporation at high temperature, and the enrichment of Si content due to the increased annealing temperature. The latter may be understood in the context of the phase diagram of bulk Si and Ge (see Figure S2 in the Supporting Information). For temperatures greater than the solidus, Si- and Ge-rich compositions of Si_xGe_{1-x} are obtained. Although phase diagrams for bulk materials require the system be at equilibrium, and thus do not apply directly to the present composites, these relationships may be used as a qualitative guide to anticipate trends in composition. Processing at lower temperatures is expected to facilitate incorporation of Ge into the NCs consistent with the present observations.

Narrowed reflections of increased intensity are noted for all reflections with increasing processing temperature (see Figure 2 for the evolution of the (220) reflection from TOP-prepared samples). These observations stem from an increase in crystallinity and size of the oxide-embedded nanodomains with temperature as previously noted for Si-NCs from HSQ.[28,37,38] In addition, the relative intensity of the Si_xGe_{1-x} reflections increases from 800 to 1050 °C. It is reasonable this results from the formation of more Si_xGe_{1-x} nanodomains arising from dissolution of Ge into Si.

For the peak processing temperature range 1050 to 1100 °C, the relative intensity of the Si_xGe_{1-x} reflection decreases substantially relative to the silicon reflection, counter to the trend observed for processing at 800 to 1050 °C. We also observe the Si_xGe_{1-x} reflections broaden relative to those of Si, consistent with a decrease in Si_xGe_{1-x} crystallite size. We ascribe these observations to the loss of Ge by evaporation.[39] A slight shift in the Si-rich reflection is also noted in Figure 1b, from 47.4° at 800 °C to 47.1° at 1100 °C consistent with the incorporation of small amounts of Ge into the Si-rich phase at higher temperatures.

The alkyl chain length of the trialkylphosphine ligand used in the Ge precursor adduct influences the relative intensity and position of the Ge-rich and Si-rich NC XRD reflections. Composites prepared using the TBP:GeI_2 adduct exhibit reflections of lower intensity (relative to the amorphous oxide signal at ca. 22°) and greater breadth than TOP-prepared samples, consistent with the formation of smaller NCs (Figure 2c). Organic modification of $SiO_{1.5}$ sol–gel polymers can interfere with Si-NC formation.[33] This observation has been attributed to carbon impurities in the matrix limiting NC growth and crystallization. However, this interpretation is not consistent with the present observations of smaller nanodomains in TBP-prepared samples, because more carbon incorporation would be expected for the TOP-prepared samples. This may arise because larger alkyl chains of TOP could lead to the formation of a more porous oxide matrix that would facilitate NC growth through enhanced diffusion.

TBP-prepared samples were evaluated as a function of increasing annealing time at 1100 °C (Figure 2d). A slight increase in Ge content is observed with increasing annealing time that is coincident with a decrease in the intensity of the Si_xGe_{1-x} reflections compared to those of the Si-rich species; this is consistent with a loss of Ge from the Ge-rich region.

dx.doi.org/10.1021/cm202761k | *Chem. Mater.* 2011, 23, 5096–5103

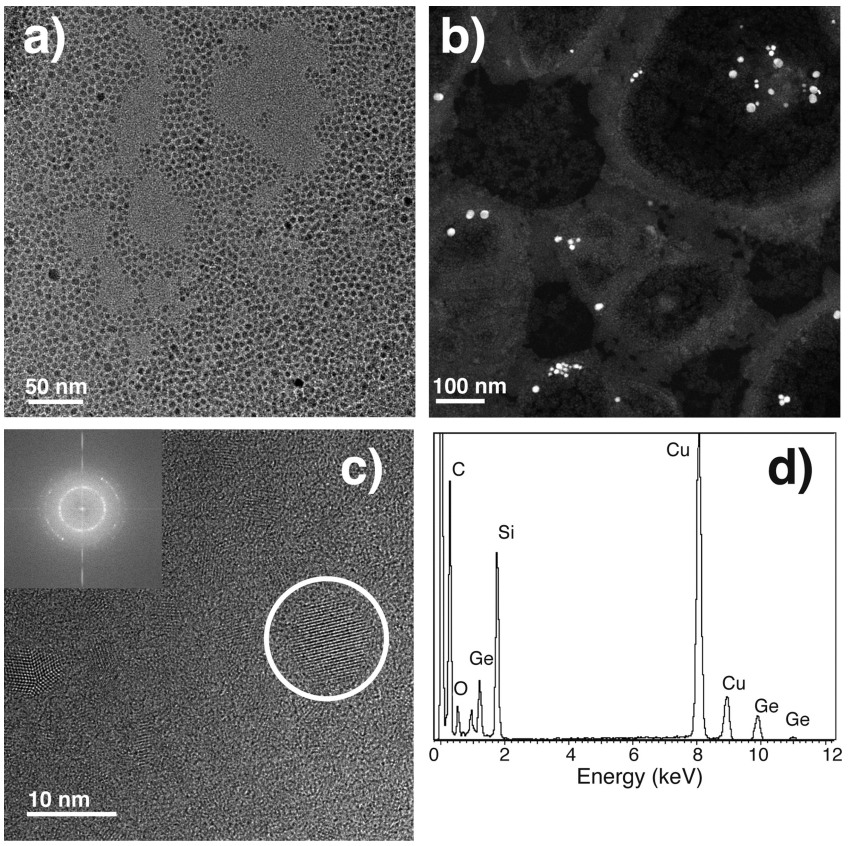

Figure 3. (a) Bright-field TEM of functionalized Si-rich and Ge-rich alloy nanoparticles from TBP-prepared composite annealed at 1100 °C (sample F). (b) HAADF highlighting a subpopulation with higher Z-contrast. (c) HRTEM showing a crystalline nanoparticle with lattice fringes consistent with a diamond structure. The circled NC had a lattice spacing of 3.2 Å, consistent with the (111) plane from a Si_xGe_{1-x} lattice of approximate $Si_{0.5}Ge_{0.5}$ composition (inset: FFT image of the HRTEM, indicating diamond-type *d*-spacing). (d) EDS showing the presence of Si and Ge (the Cu, C, and O signals arise from the grid).

Although XRD characterization of the present systems gives insight into the impact of the key processing parameters on particle size and composition, it is challenging to draw definitive conclusions regarding NC morphology. As well, overlapping of the Ge- and Si-rich reflections, and the possibility of other factors including phase segregation[40] and/or strain contributing to reflection broadening, makes estimation of size by Scherrer analysis potentially unreliable. The present XRD observations could be interpreted in the context of several possible nanodomain motifs:

(1) each NC contains distinct Si-rich and Ge-rich regions that are randomly structured,
(2) each NC contains distinct Si-rich and Ge-rich alloy regions that are well-defined (e.g., core−shell structure), or
(3) a heterogeneous mixture of Si-rich and Ge-rich NCs exists within the composite.

HRTEM and HAADF imaging were used to determine the type of motif present in these samples. HF etching of samples A and F removed the oxide matrix, facilitating HRTEM characterization of the resulting freestanding NCs. The liberated particles were functionalized with 1-dodecene via thermal hydrosilylation/hydrogermylation at 190 °C. FTIR spectroscopy of the HF-etched materials shows an intense feature centered at ca. 2080 cm^{-1} consistent with the formation of $Si-H_x$ and $Ge-H_x$ species (see the Supporting Information, Figure S3).[41] Following functionalization, vibrations associated with the grafted alkyl chains are noted at ca. 2950 ($-CH_3$ stretch) and 1465 cm^{-1} ($-CH_2$ bend) and a broadened $Si-H_x$/$Ge-H_x$ stretch feature centered at 2084 cm^{-1} of substantially reduced in intensity are observed. A low-intensity Si−O−Si feature at ca. 1050 cm^{-1} arising from trace surface oxidation is also noted.

Figure 3 shows a bright-field TEM image of TBP-prepared particles annealed at 1100 °C after functionalization. HRTEM lattice fringes matching the *d*-spacings observed by XRD of the oxide-composites are evident, clearly showing the crystalline nature of the nanoparticles. Fast Fourier transform (FFT) analysis of the HRTEM image showed ensemble characteristic (111) *d*-spacing ranging from ca. 3.3−3.15 Å, which is consistent with the lattice spacing in elemental Si (3.13 Å) and elemental Ge (3.27 Å), and the ensemble phases identified by powder XRD. A bimodal distribution of particle sizes is evident, with a distribution of 5.9 ± 1.0 (N = 545) nm particles and a second mode at 10.9 ± 3.6 nm (N = 52).

To determine the distribution of Ge within these populations, the NCs were analyzed by HAADF and EDS line scanning, which enhances contrast between Si and Ge within the particles. Compared to the bright field micrographs, HAADF images highlight a subpopulation of particles ca. 10−20 nm in diameter with higher Z-contrast indicating an enriched Ge content. Another population of smaller particles with lower contrast is also noted. An EDS line scan of a representative ca. 12 nm particle from the high Z-contrast population indicates Si and Ge are homogeneously distributed

dx.doi.org/10.1021/cm202761k | *Chem. Mater.* 2011, 23, 5096−5103

thoughout the particle (Figure 4). An EDS line scan of a ca. 5 nm particle with low Z-contrast shows predominately Si, with

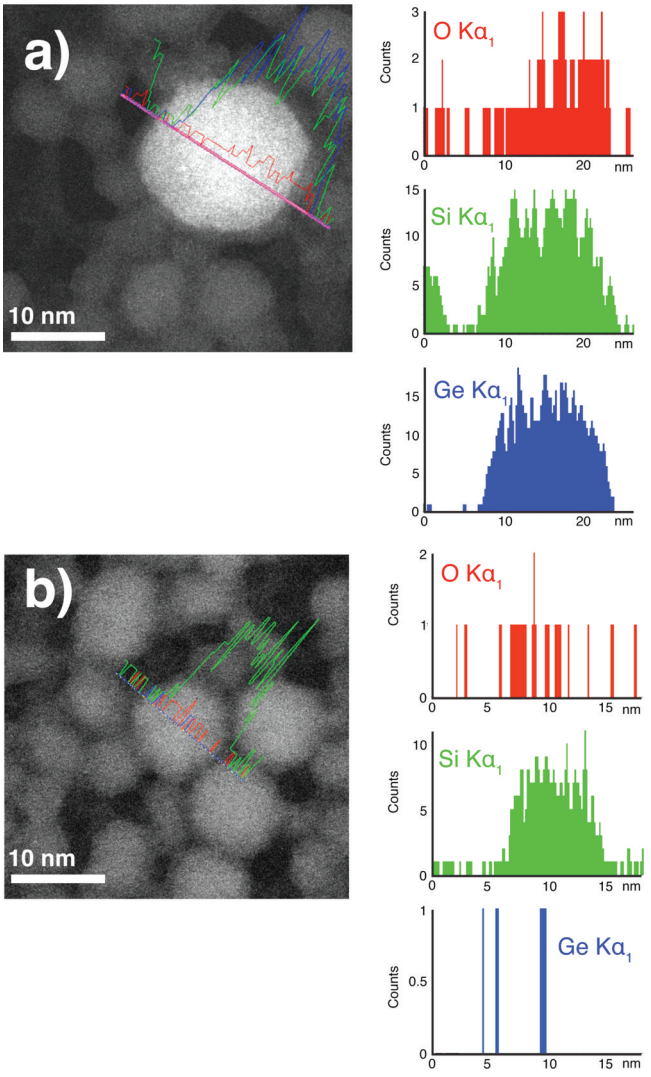

Figure 4. (a) HAADF of a 12 nm Ge-rich NC (prepared from sample A). EDS line scanning indicated a uniform distribution of Si (green) and Ge (blue) within the particle, with a small quantity of O (red) present. (b) HAADF of 5 nm Si-rich NC (prepared from sample A). EDS line scanning showed the particle consists of largely Si (green), with only trace amounts of O (red) or Ge (blue) present.

low quantities of Ge and O. EDS quantification at selected points within these populations showed Ge compositions of ca. 53 and 0.3%, respectively.

These microscopy results confirm a bimodal particle size distribution with two separate Si_xGe_{1-x} populations: a larger diameter Ge-rich population and a smaller diameter Si-rich population. This is fully consistent with our XRD patterns (Figure 2) that clearly show two separate populations with different alloy compositions, one with significantly increased Ge content.

We propose the bimodal distribution of Ge-rich and Si-rich NCs arises through the influence of the GeI_2:PR_3 adduct on NC nucleation and growth. During the rearrangement processes of HSQ and GeI_2 at ca. 300−400 °C,[28] R_3P:GeI_2 adduct decomposition products could serve as heterogeneous nucleation sites for Ge-rich Si_xGe_{1-x} NCs. Any remaining Si or Ge suboxide species that do not participate in the initial nucleation would remain available for subsequent diffusion into the Si-rich NC population, which has been previously identified as the major growth mechanism for Si-NCs from pure HSQ.[37] The XRD and EDS line scan results are consistent with small quantities of Ge incorporated into the smaller, Si-rich particles, though detection of Ge in these particles is near the limit for both methods. Incorporation of Ge into each phase is also qualitatively consistent with PL characterization (vide infra).

Oxide composites annealed from 1000 to 1100 °C exhibit near-IR PL red-shifted in comparison to PL from Si-NC prepared using HSQ (Figure 5). Representative Si_xGe_{1-x}

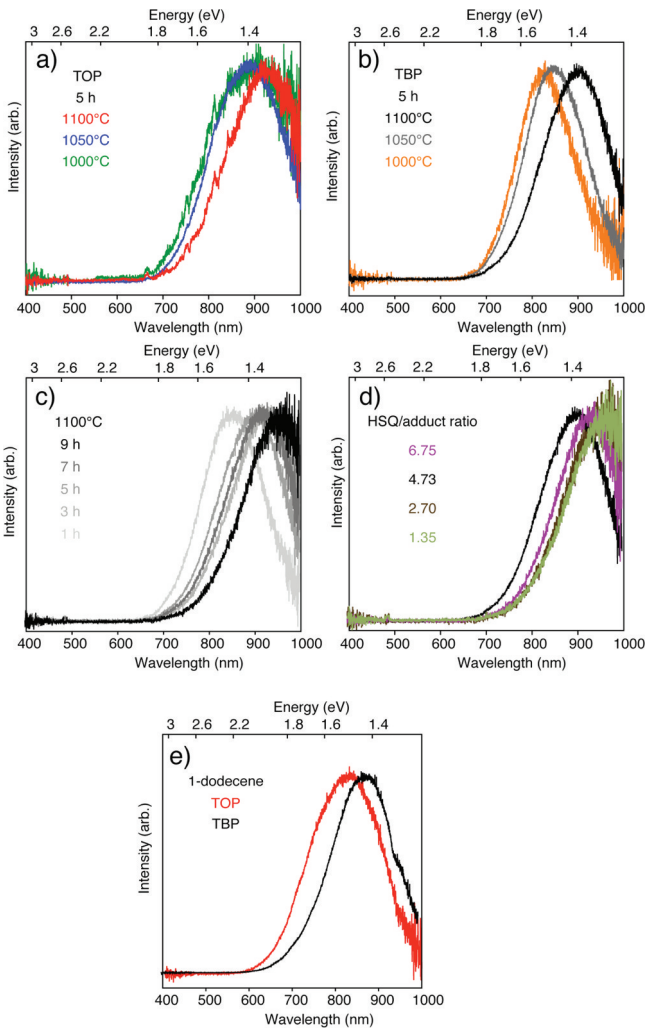

Figure 5. PL spectra (λ_{ex} 457 nm) of (a) TOP-prepared composites processed from 1000 to 1100 °C (A−C). (b) TBP-prepared composites processed from 1000 to 1100 °C (F−H). (c) TBP-prepared composites processed at 1100 °C from 1 to 9 h (I−L). (d) TBP-prepared samples at 1100 °C with varying HSQ loading (M−O). (e) Functionalized NCs prepared from TOP-prepared composite A and TBP-prepared composite F.

samples show red-shifts with increasing temperature processing from 1000 to 1100 °C, with PL maxima shifting from ca. 820 to 915 nm for TOP-prepared samples and ca. 830−923 nm for TBP-prepared samples. For comparison, HSQ annealed at 1100 °C under the identical processing conditions (i.e., 5 h annealing time) exhibited a PL maximum at 880 nm (not shown).

dx.doi.org/10.1021/cm202761k|*Chem. Mater.* 2011, 23, 5096−5103

The observation of red-shifted PL is qualitatively consistent with Ge incorporation into luminescent Si_xGe_{1-x} NCs. However, it is important to note the red-shift could arise from several factors related to the interdependent changes in NC size and composition that result from the processing conditions described above. The possibility of PL from both Ge-rich and Si-rich populations is also a complicating factor. We are actively pursuing other techniques including X-ray excited optical luminescence (XEOL) spectroscopy that provide the elemental specificity required to characterize the chemical environment of the emissive species in these materials.[42]

Although the present XRD results suggest increasing processing temperature decreases the Ge content in the Si_xGe_{1-x} NCs (expected to blue-shift the PL), doing so also increases NC size (which may account for the observed PL red-shift). Increased Ge content by adjusting the germanium adduct:HSQ ratio in the precursor for TBP samples processed at 1100 °C resulted in a red-shift from ca. 929 to 962 nm, a trend consistent with compositional effects decreasing the bandgap. Extended annealing of TBP-prepared samples at 1100 °C from 1 to 9 h resulted in a red-shift from to ca. 850 to 950 nm a trend previously noted for Si-NCs derived from HSQ and attributed to activation of larger NCs through defect passivation.[32] The red-shifted PL from both TOP- and TBP-prepared samples compared to composites prepared using pure HSQ goes against the trend expected from carbon impurities from phosphine decomposition. Recall, carbon impurities were previously observed to lead to smaller nanodomains and a blue-shift in PL.[33]

Interestingly, hydride-terminated particles isolated directly from the HF etching process do not exhibit any detectable PL; following hydrosilylation, NCs derived from composites samples prepared using TOP and TBP adducts exhibit intense PL centered at ca. 825 and 880 nm, respectively (blue-shifted from the corresponding oxide composite PL). Functionalized NCs exhibited PL quantum yields of 16 ± 3%, compared to 18 ± 3% for similarly functionalized 1100 °C-processed Si-NCs from HSQ. Pi and Kortshagen studied 3 nm freestanding Si_xGe_{1-x}-NCs prepared by a nonthermal plasma, suggesting composition did not appreciably shift the bandgap and attributed this to a Si-like band structure.[27] Instead, they noted increased Ge incorporation lead to a loss of PL intensity, attributed to the formation of Ge-related surface defects. In comparison, hydride-terminated Si-NCs prepared from HSQ exhibit intense PL consistent with quantum confinement effects.[37] Therefore, the present observation of HF-induced loss of PL response is qualitatively consistent with $Ge-H_x$ related surface defects that are passivated upon thermal hydrogermylation. Furthermore, the relatively high photoluminescent quantum yields of the present materials are comparable to Si-NCs of similar size and surface-chemistry. This indirectly suggests that Ge plays an active role in the emission process. If all Ge-containing NCs were non-luminescent, it would substantially reduce the quantum yield through competitive absorption.

CONCLUSION

We have conducted a comprehensive investigation into the use of $R_3P:GeI_2$ adducts with HSQ to form oxide-embedded and freestanding Si_xGe_{1-x} NCs. Through changes to processing temperature, time, processing atmosphere and precursor stoichiometry, the Ge composition could be shifted from 64 − 86%. The particle morphology was confirmed using HRTEM and EDS linescanning. Through this analysis, it was shown this synthesis forms a heterogeneous mixture of Ge- and Si-rich NCs. A multistep formation mechanism was proposed, in which the germanium precursor helps nuleate larger Si_xGe_{1-x} NCs. A separate population of Si-rich NCs are also formed through matrix diffusion, and may also incorporate low amounts of Ge through matrix diffusion processes. However, Ge incorporation in both populations may be limited by evaporation of volatile Ge species during annealing.

The near-IR PL exhibited by the oxide composites and functionalized materials was evaluated, and Ge incorporation was qualitatively demonstrated to shift the optoelectronic properties. The promising near-IR PL of Si_xGe_{1-x}-NCs (with a maximum wavelength of 962 nm and quantum yield comparable to Si-NCs in the present system) may be of interest in applications including biological tags or CMOS devices. We are developing further improvements to this synthetic approach to minimize heterogeneity (for example, through the use of size-selective photochemical functionalization[43] or density gradient ultracentrifugation[44]) to allow greater insight into the impact of Ge alloying on the optoelectronic properties.

ASSOCIATED CONTENT

Supporting Information

Calculated lattice constants, wide-angle XRD patterns for all of composite samples, details of compositional calculation using a modified version of Vegard's law, FTIR of freestanding particles, TEM size distribution histogram. This material is available free of charge via the Internet at http://pubs.acs.org

AUTHOR INFORMATION

Corresponding Author

*Fax: 780-492-8231. Tel: 780-492-7206. E-mail: jveinot@ualberta.ca.

Present Address

[†]Lash Miller Chemical Laboratories, Department of Chemistry, University of Toronto, 80 St- George Street, Toronto, ON, M5S 3H6, Canada.

ACKNOWLEDGMENTS

The authors acknowledge funding from the Natural Sciences and Engineering Research Council of Canada (NSERC), Canada Foundation for Innovation (CFI), Alberta Science and Research Investment Program (ASRIP), Alberta Innovates: Technology Futures, and University of Alberta Department of Chemistry. M. Dermott and N. Yang are thanked for assistance with Raman spectroscopy. A. Meldrum is thanked for access to laser systems to evaluate photoluminescence spectroscopy. C. Andrei and the Brockhouse Institute for Materials Research are thanked for HRTEM imaging. A. Midgett and M. Beard at the National Renewable Energy Laboratory are thanked for assistance with the absolute quantum yield measurements.

REFERENCES

(1) Michalet, X.; Pinaud, F. F.; Bentolila, L. A.; Tsay, J. M.; Doose, S.; Li, J. J.; Sundaresan, G.; Wu, A. M.; Gambhir, S. S.; Weiss, S. *Science* **2005**, *307*, 538−544.

(2) Liu, H.; Winkenwerder, W.; Liu, Y. R.; Ferrer, D.; Shahrjerdi, D.; Stanley, S. K.; Ekerdt, J. G.; Banerjee, S. K. *Ieee Trans. Electron Devices* **2008**, *55*, 3610−3614.

(3) Akca, I. B.; Dana, A.; Aydinli, A.; Turan, R. *Appl. Phys. Lett.* **2008**, *92*, 052103.
(4) Rossetti, R.; Nakahara, S.; Brus, L. E. *J. Chem. Phys.* **1983**, *79*, 1086−1088.
(5) Bawendi, M. G.; Steigerwald, M. L.; Brus, L. E. *Annu. Rev. Phys. Chem.* **1990**, *41*, 477−496.
(6) Zhong, X. H.; Feng, Y. Y.; Zhang, Y. L.; Gu, Z. Y.; Zou, L. *Nanotechnology* **2007**, *18*, 385606, 6pp.
(7) Swafford, L. A.; Weigand, L. A.; Bowers, M. J.; McBride, J. R.; Rapaport, J. L.; Watt, T. L.; Dixit, S. K.; Feldman, L. C.; Rosenthal, S. J. *J. Am. Chem. Soc.* **2006**, *128*, 12299−12306.
(8) Choi, Y. J.; Hwang, I. S.; Park, J. H.; Nahm, S.; Park, J. G. *Nanotechnology* **2006**, *17*, 3775−3778.
(9) Kuno, M.; Higginson, K. A.; Qadri, S. B.; Yousuf, M.; Lee, S. H.; Davis, B. L.; Mattoussi, H. *J. Phys. Chem. B* **2003**, *107*, 5758−5767.
(10) Bailey, R. E.; Nie, S. M. *J. Am. Chem. Soc.* **2003**, *125*, 7100−7106.
(11) Regulacio, M. D.; Han, M. Y. *Acc. Chem. Res.* **2010**, *43*, 621−630.
(12) Zhong, X. H.; Han, M. Y.; Dong, Z. L.; White, T. J.; Knoll, W. *J. Am. Chem. Soc.* **2003**, *125*, 8589−8594.
(13) Wang, X. Y.; Ren, X. F.; Kahen, K.; Hahn, M. A.; Rajeswaran, M.; Maccagnano-Zacher, S.; Silcox, J.; Cragg, G. E.; Efros, A. L.; Krauss, T. D. *Nature* **2009**, *459*, 686−689.
(14) Nirmal, M.; Dabbousi, B. O.; Bawendi, M. G.; Macklin, J. J.; Trautman, J. K.; Harris, T. D.; Brus, L. E. *Nature* **1996**, *383*, 802−804.
(15) Kuno, M.; Fromm, D. P.; Hamann, H. F.; Gallagher, A.; Nesbitt, D. J. *J. Chem. Phys.* **2001**, *115*, 1028−1040.
(16) Palfinger, G.; Bitnar, B.; Sigg, H.; Muller, E.; Stutz, S.; Grutzmacher, D. *Phys. E* **2003**, *16*, 481−488.
(17) Sunamura, H.; Shiraki, Y.; Fukatsu, S. *Appl. Phys. Lett.* **1995**, *66*, 953−955.
(18) Yang, L. F.; Watling, J. R.; Wilkins, R. C. W.; Borici, M.; Barker, J. R.; Asenov, A.; Roy, S. *Semicond. Sci. Technol.* **2004**, *19*, 1174−1182.
(19) Virgilio, M.; Grosso, G. *J. Phys.: Condens. Matter* **2006**, *18*, 1021−1031.
(20) Takeoka, S.; Toshikiyo, K.; Fujii, M.; Hayashi, S.; Yamamoto, K. *Phys. Rev. B* **2000**, *61*, 15988−15992.
(21) Asaduzzaman, A. M.; Springborg, M. *Phys. Rev. B* **2006**, *74*, 165406, 7pp.
(22) Rehman, H.; Springborg, M.; Dong, Y. *J. Phys. Chem.* **2011**, *115*, 2005−2015.
(23) Walker, B. G.; Hendy, S. C.; Tilley, R. D. *Eur. Phys. J. B* **2009**, *72*, 193−201.
(24) Tang, Y. S.; Cai, S.; Jin, G.; Duan, J.; Wang, K. L.; Soyez, H. M.; Dunn, B. S. *Appl. Phys. Lett.* **1997**, *71*, 2448−2450.
(25) Hwang, C. W.; Ryu, M. K.; Kim, K. B.; Lee, S. C.; Kim, C. S. *J. Appl. Phys.* **1995**, *77*, 3042−3047.
(26) Yang, Y. M.; Wu, X. L.; Siu, G. G.; Huang, G. S.; Shen, J. C.; Hu, D. S. *J. Appl. Phys.* **2004**, *96*, 5239−5242.
(27) Pi, X. D.; Kortshagen, U. *Nanotechnology* **2009**, *20*, 295602, 6 pp.
(28) Henderson, E. J.; Veinot, J. G. C. *Chem. Mater.* **2007**, *19*, 1886−1888.
(29) Kelly, J. A.; Henderson, E. J.; Veinot, J. G. C. *Chem. Commun.* **2010**, *46*, 8704−8718.
(30) Jackson, H. L.; Mccormac, Wb; Rondestv, Cs; Smeltz, K. C.; Viele, I. E. *J. Chem. Educ.* **1970**, *47*, A175−A188.
(31) Semonin, O. E.; Johnson, J. C.; Luther, J. M.; Midgett, A. G.; Nozik, A. J.; Beard, M. C. *J. Phys. Chem. Lett.* **2010**, *1*, 2445−2450.
(32) Hessel, C. M.; Henderson, E. J.; Veinot, J. G. C. *J. Phys. Chem. C* **2007**, *111*, 6956−6961.
(33) Henderson, E. J.; Kelly, J. A.; Veinot, J. G. C. *Chem. Mater.* **2009**, *21*, 5426−5434.
(34) Cronemeyer, D. C. *J. Appl. Phys.* **1958**, *29*, 1730−1735.
(35) King, R. B. *Inorg. Chem.* **1963**, *2*, 199−200.
(36) Lu, X. M.; Korgel, B. A.; Johnston, K. P. *Chem. Mater.* **2005**, *17*, 6479−6485.
(37) Hessel, C. M.; Henderson, E. J.; Veinot, J. G. C. *Chem. Mater.* **2006**, *18*, 6139−6146.
(38) Henderson, E. J.; Seino, M.; Puzzo, D. P.; Ozin, G. A. *ACS Nano* **2010**, *4*, 7683−7691.
(39) Searcy, A. W. *J. Am. Chem. Soc.* **1952**, *74*, 4789−4791.
(40) Mogaddam, N. A. P.; Alagoz, A. S.; Yerci, S.; Turan, R.; Foss, S.; Finstad, T. G. *J. Appl. Phys.* **2008**, *104*, 124309, 6pp.
(41) Buriak, J. M. *Chem. Rev.* **2002**, *102*, 1271−1308.
(42) Kelly, J. A.; Henderson, E. J.; Clark, R. J.; Hessel, C. M.; Cavell, R. G.; Veinot, J. G. C. *J. Phys. Chem. C* **2010**, *114*, 22375−22790.
(43) Kelly, J. A.; Shukaliak, A. M.; Fleischauer, M. D.; Veinot, J. G. *J. Am. Chem. Soc.* **2011**, *133*, 9564−9571.
(44) Mastronardi, M. L.; Hennrich, F.; Henderson, E. J.; Maier-Flaig, F.; Blum, C.; Reichenbach, J.; Lemmer, U.; Kübel, C.; Wang, D.; Kappes, M. M.; Ozin, G. A. *J. Am. Chem. Soc.* **2011**, *133*, 11928−11931.